

A BOUNDARY INTEGRAL METHOD FOR COMPUTING THE DYNAMICS OF AN EPITAXIAL ISLAND*

SHUWANG LI[†] AND XIAOFAN LI[‡]

Abstract. In this paper, we present a boundary integral method for computing the quasi-steady evolution of an epitaxial island. The problem consists of an adatom diffusion equation (with desorption) on terrace and a kinetic boundary condition at the step (island boundary). The normal velocity for step motion is determined by a two-sided flux. The integral formulation of the problem involves both double- and single-layer potentials due to the kinetic boundary condition. Numerical tests on a growing/shrinking circular or a slightly perturbed circular island are in excellent agreement with the linear analysis, demonstrating that the method is stable, efficient, and spectrally accurate in space. Nonlinear simulations for the growth of perturbed circular islands show that sharp tips and flat edges will form during growth instead of the usual dense branching morphology seen throughout physical and biological systems driven out of equilibrium. In particular, Bales–Zangwill instability is manifested in the form of wave-like fronts (meandering instability) around the tip regions. The numerical techniques presented here can be applied generally to a class of free/moving boundary problems in physical and biological science.

Key words. integral equation, epitaxial thin film, potential theory, free or moving boundary problems, island dynamics

AMS subject classifications. 65M38, 65M80, 65R20

DOI. 10.1137/100814871

1. Introduction. Epitaxial crystal growth by depositing atoms from a gas phase onto a substrate is a nonequilibrium process involving both kinetics and thermodynamics [1, 2, 8]. At the early stages of growth, adatoms on the substrate often form small isolated islands [3, 4]. The morphological evolution (e.g., growth or shrinkage) of these islands is determined by many physical processes such as atom adsorption and desorption, adatom diffusion, and adatom attachment to island boundaries or detachment from the boundaries [1, 5, 6, 2]. Mathematical formulation of the problem leads to a moving boundary/interface problem with island boundaries as the moving interfaces. Modeling and characterizing the morphology and dynamics of these islands has long been a challenging topic in the research community of materials science and mathematics [7, 8, 9, 10, 12, 13, 16, 19, 20, 21, 22, 23, 24, 28, 31, 27].

In 1951, Burton, Cabrera, and Frank (BCF) first formulated a model to describe the dynamics of epitaxial growth [7]. In their model, the growth direction is discrete and the velocity at the moving steps is determined by a diffusion flux of adatoms attached to the step edges. On the terrace, however, a continuous function describing the adatom density is used to solve a diffusion equation subject to a thermodynamic equilibrium boundary condition. A major insight of the BCF model is that crystal growth is now viewed as a flow of the ledges or steps. Thus, the BCF model provides

*Submitted to the journal's Computational Methods in Science and Engineering section November 15, 2010; accepted for publication (in revised form) September 9, 2011; published electronically November 29, 2011. Some computations in this work were performed on computers acquired using NSF grant (SCREMS) DMS-0923111.

<http://www.siam.org/journals/sisc/33-6/81487.html>

[†]Corresponding author. Department of Applied Mathematics, Illinois Institute of Technology, Chicago, IL 60616 (sli@math.iit.edu). This author's research was supported by NSF grant DMS-0914923.

[‡]Department of Applied Mathematics, Illinois Institute of Technology, Chicago, IL 60616 (lix@iit.edu).

a framework for studying the nonequilibrium evolutions of crystal surfaces. Later, the boundary conditions have been modified to include more physics. One example is the Ehrlich–Schwoebel energy barrier that an adatom at the upper terrace experiences in order to move down to the lower terrace [29, 30]. The resulting mismatch or asymmetry in the attachment and detachment rate of adatoms due to Ehrlich–Schwoebel barrier gives rise to the Bales–Zangwill instability for the evolution of straight steps [16]. This semidiscrete step flow model has been largely used to describe the atomistic mechanisms of growth.

Recently, Cafisch et al. reformulated the boundary condition at a step (island boundary) and proposed a kinetic step model by adding kinetics, i.e., adatoms attach to steps at a finite rate, and there is no near-equilibrium assumptions in the model [11, 12]. Using such a kinetic model, Li, Rätz, and Voigt (LRV) studied the linear stability of an isolated circular epitaxial island [25]. In their calculation, the island is situated in a large, fixed circle with a zero flux boundary condition and there is no desorption of adatoms. LRV found that when the line tension is present, islands are always stable. This indicates that the Bales–Zangwill instability for straight steps due to the asymmetry in the attachment and detachment rate of adatoms does not occur for small islands (in the linear regime).

More recently, Hu, Li, and Lowengrub (HLL) extended the study of LRV to include a more complete set of physical parameters, especially desorption [20]. They performed a comprehensive morphological stability analysis of a single, epitaxially growing, perturbed circular island and suggested a way to control the shape of the island using a deposition flux and a far-field flux as control variables. In [20], the linear stability analysis reveals that there exists critical conditions, a time-dependent deposition flux $\Lambda^c(t)$, below which the island will shrink and above which the island will grow. This deposition flux depends on the desorption rate of adatoms, the line tension of the island, and the size of the island. Here, we will develop a boundary integral method to characterize the nonlinear morphological stability of an island.

Many computational methods have been developed for simulating the epitaxial growth, such as the level set methods (e.g., see [36, 45, 13, 14, 15]), front-tracking methods (e.g., see [22, 38]), immersed interface methods (e.g., see [32]), as well as phase field methods (e.g., see [23, 24, 26]). These methods are usually coupled with adaptive mesh algorithms and multigrid solvers to gain more efficiency. When applicable (e.g., for piecewise homogeneous problems) boundary integral methods are typically the most efficient and accurate methods for simulating interface dynamics because the dimensionality of the problem is reduced by one and there are well-developed accurate and stable discretizations of boundary integral equations. Further, while boundary integral methods are important in their own right, they can also serve as benchmarks for other more general methods. Somewhat surprisingly, very limited studies based on boundary integral equations have been developed for the epitaxial crystal growth problem. In [17], Liu and Metiu used a Green’s function approach to analyze the linear behavior of a step train; in [33], Huang, Lai, and Xiang developed an integral approach based on spectral deferred correction techniques. To the best of our knowledge, none of the previously published works includes adatom desorption, which is one of the major processes involved in epitaxial growth [1, 2, 49, 47, 48] and sometimes unavoidable for vapor deposition growth [47].

In this paper, we study a fundamental problem: the growth and shrinkage of a monolayer island on a large substrate. In particular, we include desorption in our model and investigate the nonlinear morphological instability at early stage of growth/shrinkage. This problem is of importance since the arrangement of adatoms

at early stages determines the final macroscopic characteristics and perfection of the crystal. Note that at the early growth, islands are usually small and widely separated [3, 4]. So we neglect the interactions among islands and focus our study on a single island. Within the context of the BCF model, we formulated the morphological evolution of the island as a moving boundary problem. In the present macroscopic description, the interface (step or island boundary) is considered as mathematically sharp. On the interface, we consider a kinetic boundary condition [25, 20]. At the far-field, we consider a zero flux boundary condition [25, 20]. Here we assume the island evolution is quasi-steady, i.e., the time scale for adatoms diffusion is much smaller than the time scale for step motion. Thus, on the terrace, the diffusion equation reduces to a modified Helmholtz equation.

A direct formulation of the proposed island problem yields an integral equation involving both double- and single-layer potentials with the adatom density as the unknown. The integral equation is solved iteratively using GMRES [51]. The interface is updated using a second-order accurate nonstiff updating scheme in time and equal arclength parameterization [39]. Note that we only solve the adatom density at the island boundary, hence dramatically reducing the total number of unknowns when compared with finite difference and finite element methods. Though the discretization of integral operators leads to dense matrices, there are fast and adaptive solvers developed for a modified Helmholtz equation in two dimensions; see [34, 35].

Our numerical tests on a growing/shrinking island are in excellent agreement with analytical predictions of linear theory and demonstrate that the method is stable, efficient, and spectrally accurate in space. Nonlinear simulations of a perturbed circular island show that (1) for deposition flux $\Lambda < \Lambda^c$, all perturbations are smoothed out and high wavenumbers (high curvature regions) are damped faster than the low wave frequencies, as expected; (2) for deposition flux $\Lambda > \Lambda^c$, shape perturbations grow rapidly at the beginning and the tip region grows faster than the trough region, and thus sharp corners form. At later times, shape perturbations exhibit oscillatory behaviors. During growth, the curvature at the tip also shows oscillatory behaviors, while the curvatures around the center of trough regions converge to zero monotonically, indicating the formation of straight edges. However, the evolution of regions close to tips shows the development of wave-like fronts, indicating the occurrence of meandering instability. Note that the tip-splitting events, which lead to usual dense branching morphology seen throughout physical and biological systems driven out of equilibrium, do not occur here.

The rest of the paper is organized as follows. In section 2, we review the governing equations for an exterior moving interface problem; in section 3, we present the numerical methods; in section 4, we discuss numerical results; and in section 5, we give conclusions.

2. Mathematical formulation.

2.1. The BCF model. Consider an isolated island epitaxially evolving on a large crystal surface (substrate). The island is one atomic layer higher than the substrate surface and expands or shrinks as time progresses. We denote the interior region occupied by the island (the upper terrace) by $\Omega_2(t)$ and the exterior substrate (the lower terrace) by $\Omega_1(t)$. The island boundary, $\Sigma(t)$, also known as the interface, separates the upper and lower terraces. Let $\rho_i = \rho_i(x, y, t)$ denote the adatom density on the upper terrace ($i = 2$) and the lower terrace ($i = 1$). Without the presence of island nucleation, the transport of adatoms on the terraces is realized through

diffusion and desorption [7, 1],

$$(2.1) \quad \partial_t \rho_i - \nabla \cdot (D \nabla \rho_i) = F - \tau^{-1} \rho_i \quad \text{for } \mathbf{x} \in \Omega_i,$$

where $D > 0$ is the diffusion coefficient (assumed to be isotropic for all terraces), F is the deposition flux rate which can be generalized as a time-dependent function, and τ^{-1} is the desorption rate. τ describes the mean life span of adatoms on the terrace before they escape back into the vapor phase. At the interface $\Sigma(t)$, the adatom density ρ satisfies kinetic boundary conditions with a curvature correction via the Gibbs–Thomson relation [25, 11, 12],

$$(2.2) \quad -D \nabla \rho_2 \cdot \mathbf{n} = k_+ (\rho_2 - \rho^* (1 + \sigma \kappa)) \quad \text{for } \mathbf{x} \in \Sigma(t),$$

$$(2.3) \quad D \nabla \rho_1 \cdot \mathbf{n} = k_- (\rho_1 - \rho^* (1 + \sigma \kappa)) \quad \text{for } \mathbf{x} \in \Sigma(t),$$

where \mathbf{n} is the unit normal of the boundary $\Sigma(t)$ pointing from the upper to the lower terrace, k_+ and k_- are the kinetic attachment rate of the adatoms to $\Sigma(t)$ from the upper and lower terraces, respectively, ρ^* is the equilibrium value of the adatom density at steady state for a straight step, σ is the line tension, and κ is the curvature of $\Sigma(t)$ and $\kappa > 0$ for a convex curve (e.g., a circle). Note that we neglect the usual convection term (see, for example, [12]), since the evolving velocity of the interface is assumed to be small in epitaxial growth. As $k_+ = k_- \rightarrow \infty$, the classical thermodynamic boundary condition (Gibbs–Thomson condition) is recovered, $\rho_i = \rho^* (1 + \sigma \kappa)$.

Without edge diffusion, the conservation of adatoms at the interface requires that the normal velocity $V(t)$ of the interface satisfy

$$(2.4) \quad V(t) = -D \nabla \rho_2 \cdot \mathbf{n} + D \nabla \rho_1 \cdot \mathbf{n} \quad \text{for } \mathbf{x} \in \Sigma(t).$$

The far-field boundary condition is specified as follows. Let the upper and the lower terraces be enclosed in a large circular far-field boundary Γ_∞ with radius $R_\infty \gg R(t)$, where $R(t)$ is the radius of an equivalent circle with the same area as the evolving island. We impose a zero flux boundary condition along Γ_∞ ,

$$(2.5) \quad \lim_{R_\infty \rightarrow \infty} \frac{1}{2\pi} \int_{\Gamma_\infty} D \nabla \rho_1 \cdot \mathbf{n} d\Gamma = 0,$$

where \mathbf{n} is the unit outward normal at Γ_∞ .

Here we assume the time scale for adatoms diffusion is much faster than the time scale for step motion and focus our study on a quasi-steady evolution case. Under this assumption, (2.1) reduces to

$$(2.6) \quad -\nabla \cdot (D \nabla \rho_i) = F - \tau^{-1} \rho_i \quad \text{for } \mathbf{x} \in \Omega_i$$

and the other equations remain unchanged. Equations (2.6) and (2.2)–(2.5) complete the description of the BCF island model and specify a nonlinear moving boundary problem.

2.2. Nondimensionalization. There are multiple lengths and time scales involved in the problem, and their relative ratios determine different growth regimes. Here we are interested in the morphological evolution of an island at early stages and choose the characteristic length scale $l^* = R(0) > 0$, where $R(0)$ is the radius of an equivalent circular disk with the same area of the island at $t = 0$. The characteristic time scale is taken to be the diffusion time scale $t^* = l^{*2}/D$, where the diffusion

coefficient D is assumed to be a constant. Note that the length scale is different from the one used in [20], where the characteristic length is taken to be R_∞ . Defining the nondimensional time and space variable $\tilde{t} = t/t^*$ and $\tilde{l} = l/l^*$, the nondimensional BCF model is given below (we drop the tilde notation):

$$(2.7) \quad -\nabla^2 \rho_i = \Lambda - \mu^2 \rho_i \quad \text{for } \mathbf{x} \in \Omega_i \quad i = 1, 2,$$

$$(2.8) \quad -\xi_+ \nabla \rho_2 \cdot \mathbf{n} = \rho_2 - \rho^*(1 + \gamma\kappa) \quad \text{for } \mathbf{x} \in \Sigma(t),$$

$$(2.9) \quad \xi_- \nabla \rho_1 \cdot \mathbf{n} = \rho_1 - \rho^*(1 + \gamma\kappa) \quad \text{for } \mathbf{x} \in \Sigma(t),$$

$$(2.10) \quad V(t) = -\nabla \rho_2 \cdot \mathbf{n} + \nabla \rho_1 \cdot \mathbf{n} \quad \text{for } \mathbf{x} \in \Sigma(t),$$

$$(2.11) \quad \lim_{R_\infty \rightarrow \infty} \frac{1}{2\pi} \int_{\Gamma_\infty} \nabla \rho_1 \cdot \mathbf{n} ds = 0,$$

where $\Lambda = \frac{Fl^{*2}}{D}$ is the nondimensional deposition flux, $\mu = \frac{l^*}{\sqrt{D\tau}}$ is the nondimensional desorption rate, $\xi_\pm = \frac{D}{k_\pm l^*}$ are the nondimensional kinetic coefficients, and $\gamma = \frac{\sigma}{l^*}$ is the nondimensional line tension.

2.3. Linear stability analysis. In this section, we perform a linear stability analysis for a slightly perturbed circular island. For simplicity, we perform our analysis on a one-side exterior problem and assume the adatom density is a constant on the upper terrace $\Omega_2(t)$. Thus, the equations we want to solve are (2.7), (2.9), (2.10), and (2.11). It is straightforward to analyze a two-sided model, and the results are qualitatively similar to the one-sided problem [20]. Though simplified, the one-sided model captures all physics involved in the problem (e.g., the Ehrlich–Schwoebel energy barrier since $k_- > k_+ = 0$) and serves as preparation for a more complete study of the epitaxial problem.

Define a modified adatom density $\omega = \rho - \frac{\Lambda}{\mu^2}$, equation (2.7) reduces to a homogeneous modified Helmholtz equation,

$$(2.12) \quad \nabla^2 \omega - \mu^2 \omega = 0 \quad \text{for } \mathbf{x} \in \Omega_1.$$

Equations (2.9), (2.10), and (2.11) become

$$(2.13) \quad \xi_- \nabla \omega \cdot \mathbf{n} = \omega + \frac{\Lambda}{\mu^2} - \rho^*(1 + \gamma\kappa) \quad \text{for } \mathbf{x} \in \Sigma(t),$$

$$(2.14) \quad V(t) = \nabla \omega \cdot \mathbf{n} \quad \text{for } \mathbf{x} \in \Sigma(t),$$

$$(2.15) \quad \lim_{R_\infty \rightarrow \infty} \frac{1}{2\pi} \int_{\Gamma_\infty} \nabla \omega \cdot \mathbf{n} ds = 0.$$

We consider a circular interface (the island boundary) perturbed by a single Fourier mode,

$$(2.16) \quad r(\alpha, t) = R(t) + \delta_m(t) \cos m\alpha,$$

where $R(t)$ is the radius of a underlying evolving circle and $\delta_m(t)$ is the dimensionless perturbation amplitude. In the following calculation, we neglect δ_m^2 and other higher order terms. By solving (2.12), (2.13), (2.14), and (2.15), we obtain the nonsingular leading order solution for modified adatom density,

$$(2.17) \quad \omega(r, t) = \frac{-\Lambda + \rho^* \mu^2 (1 + \frac{\gamma}{R})}{\mu^2 [K_0(R\mu) + \xi \mu K_1(R\mu)]} K_0(r\mu),$$

and the growth rate of $R(t)$,

$$(2.18) \quad \frac{dR}{dt} = \frac{\Lambda - \rho^* \mu^2 (1 + \gamma/R)}{\mu (K_0(R\mu) + \xi_- \mu K_1(R\mu))} K_1(R\mu),$$

where $K_0(z)$ and $K_1(z)$ are the modified Bessel functions of the second kind of order zero and one, respectively. They are defined by

$$(2.19) \quad K_0(z) = -\left(\log \frac{z}{2} + C\right) I_0(z) + \sum_{n=1}^{\infty} \frac{\psi(n)}{(n!)^2} \left(\frac{z}{2}\right)^{2n},$$

$$(2.20) \quad K_1(z) = \frac{1}{z} + \left(\log \frac{z}{2} + C\right) I_1(z) - \frac{1}{2} \sum_{n=0}^{\infty} \frac{\psi(n+1) + \psi(n)}{n!(n+1)!} \left(\frac{z}{2}\right)^{2n+1},$$

where C is the Euler constant $C = 0.57721\dots$ and $\psi(n) = \sum_{m=1}^n \frac{1}{m}$ for $n = 1, 2, \dots$. Here we set $\psi(0) = 0$. $I_0(z)$ and $I_1(z)$ are modified Bessel functions of the first kind, and they are defined by

$$(2.21) \quad I_0(z) = \sum_{n=0}^{\infty} \frac{1}{(n!)^2} \left(\frac{z}{2}\right)^{2n},$$

$$(2.22) \quad I_1(z) = \sum_{n=0}^{\infty} \frac{1}{n!(n+1)!} \left(\frac{z}{2}\right)^{2n+1}.$$

Note that Bessel functions $K_0(z)$ and $K_1(z)$ become singular when $z = 0$ and decrease exponentially when z is large, $K_i(z) = \sqrt{\frac{\pi}{2z}} e^{-z} (1 + \mathcal{O}(1/z))$, $i = 1, 2$, where notation $\mathcal{O}(1/z)$ denotes a smooth function that vanishes as $z \rightarrow \infty$.

In order to identify the regimes of growth, we set $\frac{dR}{dt} = 0$ and obtain a critical flux

$$(2.23) \quad \Lambda^c(t) = \mu^2 \rho^* \left(1 + \frac{\gamma}{R(t)}\right) > 0.$$

If the applied deposition flux Λ is larger than Λ^c , the island will grow; if the applied deposition flux Λ is less than Λ^c , the island will shrink. This is due to the effect of desorption: a certain amount of adatoms desorb into the gas phase. Thus a larger deposition flux is needed to grow the island. In the case without desorption (e.g., growth under low temperature conditions), any positive deposition flux will drive the island to grow. Notice in (2.23) that the critical flux Λ^c decreases as $R(t)$ increases (growth), and Λ^c increases as $R(t)$ decreases (shrink).

On the other hand, for a given deposition flux Λ , one can define a critical radius $R^c = \frac{\gamma \mu^2 \rho^*}{\Lambda - \mu^2 \rho^*}$ such that islands with radius $R > R^c$ will grow and islands with radius $R < R^c$ will shrink.

Next we compute the first order solution and mainly use it to test the accuracy of our numerical results. Following [37, 20], the m th mode perturbation evolves as

$$(2.24) \quad \left(\frac{\delta_m}{R}\right)^{-1} \frac{d}{dt} \left(\frac{\delta_m}{R}\right) = b_0 \mu^2 K_2(R\mu) - b_1 \mu K_{-1+m}(R\mu) - b_1 m K_m(R\mu)/R,$$

where K_2, K_{-1+m} , and K_m , are modified Bessel function of second kind of order 2, $m - 1$, and m , respectively. b_0 and b_1 are coefficients given by

$$(2.25) \quad b_0 = \frac{-R\Lambda + R\rho^*\mu^2 + \rho^*\mu^2\gamma}{R\mu^2(K_0(R\mu) + \xi_{-\mu}K_1(R\mu))},$$

$$b_1 = \frac{(-1 + m^2)\rho^*\gamma + b_0 R\mu (\xi_{-R\mu}K_0(R\mu) + (\xi_{-} + R)K_1(R\mu))}{R(\xi_{-R\mu}K_{-1+m}(R\mu) + (m\xi_{-} + R)K_m(R\mu))}.$$

Similar to the results presented in [20, 25], the perturbation $\frac{\delta_m}{R}$ decays if the applied flux $\Lambda > \Lambda^c$, i.e., the evolution of the island is stable.

3. Numerical method.

3.1. Mathematical preliminaries. In this section, we describe the arclength reference frame used to evolve the island. We assume the interface curve $\Sigma(t)$ is analytic and given by

$$(3.1) \quad \Sigma(t) = \{\mathbf{x}(\alpha, t) = (x(\alpha, t), y(\alpha, t)) : 0 \leq \alpha < 2\pi\},$$

where $\mathbf{x} : R \rightarrow R^2$ is analytic and 2π -periodic in α , and α denotes a parameterization of the $\Sigma(t)$. The unit tangent and normal vectors can be calculated using

$$(3.2) \quad \mathbf{s} = (x_\alpha, y_\alpha)/s_\alpha, \quad \mathbf{n} = (y_\alpha, -x_\alpha)/s_\alpha,$$

where the local variation of the arclength is $s_\alpha = \sqrt{x_\alpha^2 + y_\alpha^2}$. In the above, and in the remainder of the paper, subscripts denote partial derivatives. Introducing the tangent angle $\theta = \tan^{-1} \frac{y_\alpha}{x_\alpha}$, we rewrite $\mathbf{n} = (\sin \theta, -\cos \theta)$ and the curvature $\kappa = \frac{\theta_\alpha}{s_\alpha} = \theta_s$. Further, the equations of motion will be reposed in terms of the tangent angle θ and the length of the interface described in section 3.3.1.

3.2. Boundary integral formulation. In this section, we derive the boundary integral equation and discuss associated numerical methods for computing the modified adatom density ω and the normal velocity $V(\alpha, t)$. Considering the Green's function $\Phi_0(\mathbf{x}, \mathbf{x}')$ that solves the modified Helmholtz equation in free space, we formulate (2.12), (2.13), (2.14), and (2.15) in terms of a boundary integral as follows. We represent the field $\omega(\mathbf{x})$ through a combination of a double-layer and a single-layer potential (we suppress the variable t here).

$$(3.3) \quad \begin{aligned} &-\frac{1}{2}\omega(\mathbf{x}) + \int_{\Sigma(t)} \xi^{-1}\omega(\mathbf{x}')\Phi_0(\mathbf{x}, \mathbf{x}')ds(\mathbf{x}') - \int_{\Sigma(t)} \omega(\mathbf{x}')\frac{\partial\Phi_0}{\partial\mathbf{n}}(\mathbf{x}, \mathbf{x}')ds(\mathbf{x}') \\ &= \int_{\Sigma(t)} \xi^{-1} \left[\rho^*(1 + \gamma\kappa) - \frac{\Lambda}{\mu^2} \right] \Phi_0(\mathbf{x}, \mathbf{x}')ds(\mathbf{x}') \quad \text{for } \mathbf{x} \in \Sigma(t), \end{aligned}$$

where \mathbf{n} is the outward normal of the interface $\Sigma(t)$, the prime indicates quantities evaluated at the position \mathbf{x}' on the interface, and the free space Green's function $\Phi_0(\mathbf{x}, \mathbf{x}') = -\frac{1}{2\pi}K_0(\mu r)$ with $r = |\mathbf{x} - \mathbf{x}'| = \sqrt{(x(\alpha) - x(\alpha'))^2 + (y(\alpha) - y(\alpha'))^2}$. Note that (3.3) is not taking the form of the usual Fredholm integral equation because of the presence of both single-layer and double-layer terms. We rewrite (3.3) as

$$(3.4) \quad \begin{aligned} &-\frac{1}{2}\omega(\alpha) + \int_0^{2\pi} \xi^{-1}\omega(\alpha')\Phi_0(\alpha, \alpha')s_\alpha(\alpha')d\alpha' + \int_0^{2\pi} \omega(\alpha')\Phi_1(\alpha, \alpha')d\alpha' \\ &= \int_0^{2\pi} \xi^{-1} \left[\rho^*(1 + \gamma\kappa) - \frac{\Lambda}{\mu^2} \right] \Phi_0(\alpha, \alpha')s_\alpha(\alpha')d\alpha', \end{aligned}$$

where the kernels are $\Phi_0(\alpha, \alpha') = -\frac{K_0(\mu r)}{2\pi}$ and $\Phi_1(\alpha, \alpha') = h(\alpha, \alpha')K_1(\mu r)$ with the auxiliary function $h(\alpha, \alpha') = \frac{(x(\alpha') - x(\alpha))y_{\alpha'} - (y(\alpha') - y(\alpha))x_{\alpha'}}{2\pi r}$. Note that function $h(\alpha, \alpha') \sim \mathcal{O}(\alpha - \alpha')$, where $\mathcal{O}(\alpha - \alpha')$ denotes a smooth function that vanishes as $\alpha \rightarrow \alpha'$.

In deriving (3.4), we have used

$$(3.5) \quad \frac{d}{dr}K_0(r) = -K_1(r).$$

To compute $\omega(\alpha)$, we discretize the planar curve $\Sigma(t)$ using a total of N marker points with equal arclength parameterization $\alpha_j = jh$, where step size $h = 2\pi/N$ and N is a power of 2.

3.2.1. Computation of the single-layer term. In (3.4), the kernel Φ_0 has a logarithmic singularity at $\alpha = \alpha'$. It can be analyzed as follows:

$$(3.6) \quad \Phi_0(\mu r) = \frac{1}{2\pi} I_0(\mu r) \log 2 \left| \sin \left(\frac{\alpha - \alpha'}{2} \right) \right| + \frac{1}{2\pi} \left[I_0(\mu r) \log \frac{\mu r}{2 \left| \sin \left(\frac{\alpha - \alpha'}{2} \right) \right|} + C I_0(\mu r) + \sum_{n=1}^{\infty} \frac{\psi(n)}{(n!)^2} \left(\frac{\mu r}{2} \right)^{2n} \right],$$

where terms in the square brackets on the right-hand side are smooth or have removable singularity at $\alpha = \alpha'$. To see this, let $\alpha \approx \alpha'$, $r = s_\alpha |\alpha - \alpha'| \sqrt{1 + \mathcal{O}(\alpha - \alpha')} = s_\alpha |\alpha - \alpha'| (1 + \mathcal{O}(\alpha - \alpha'))$. Thus, for an analytic and periodic function $f(\alpha, \alpha')$, a standard composite trapezoidal rule or alternating point rule can be used to evaluate the integral $\int_0^{2\pi} f(\alpha, \alpha') \log \frac{\mu r}{2 \left| \sin \left(\frac{\alpha - \alpha'}{2} \right) \right|} d\alpha'$ and achieve spectral accuracy. One can also use the hybrid Gauss-trapezoid quadrature rules based on the Euler–Maclaurin formula to evaluate the integral [55].

The first term on the right-hand side of (3.6) is still singular and can be evaluated using Hilbert transform [39] or a spectrally accurate quadrature [44]

$$(3.7) \quad \int_0^{2\pi} f(\alpha_i, \alpha') \log 2 \left| \sin \left(\frac{\alpha_i - \alpha'}{2} \right) \right| d\alpha' \approx \sum_{j=0}^{2m-1} q_{|j-i|} f(\alpha_i, \alpha_j),$$

where $m = N/2$, $\alpha_i = \frac{\pi i}{m}$ for $i = 0, 1, \dots, 2m - 1$, and weight coefficients

$$(3.8) \quad q_j = -\frac{\pi}{m} \sum_{k=1}^{m-1} \frac{1}{k} \cos \frac{kj\pi}{m} - \frac{(-1)^j \pi}{2m^2} \quad \text{for } j = 0, 1, \dots, 2m - 1.$$

We also use the above quadrature to compute the right-hand side of (3.4).

3.2.2. Computation of the double-layer term. In (3.4), similar to the splitting approach used in the single-layer term, the double-layer term can be analyzed as follows:

$$(3.9) \quad \Phi_1(\mu r) = g_1(\alpha, \alpha') \log 2 \left| \sin \left(\frac{\alpha - \alpha'}{2} \right) \right| + g_2(\alpha - \alpha'),$$

where functions $g_1(\alpha, \alpha')$ and $g_2(\alpha, \alpha')$ are analytic and periodic with

$$(3.10) \quad g_1(\alpha, \alpha') = h(\alpha, \alpha') I_1(\mu r),$$

$$(3.11) \quad g_2(\alpha, \alpha') = h(\alpha, \alpha') \left[\frac{1}{\mu r} + I_1(\mu r) \log \frac{\mu r}{2 \left| \sin \left(\frac{\alpha - \alpha'}{2} \right) \right|} + C I_1(\mu r) + \frac{1}{2} \sum_{n=0}^{\infty} \frac{\psi(n+1) + \psi(n)}{n!(n+1)!} \left(\frac{\mu r}{2} \right)^{2n+1} \right].$$

We first observe that except for the first term, all other terms in the brackets in (3.11) will vanish at the singular point $\alpha = \alpha'$, i.e., $r = 0$ because $I_1(0) = 0$. For $\alpha = \alpha'$, the first term in the brackets in (3.11) can be calculated explicitly using

$$(3.12) \quad \frac{h(\alpha, \alpha)}{\mu r} = \frac{1}{4\pi\mu} \frac{x_\alpha y_{\alpha\alpha} - x_{\alpha\alpha} y_\alpha}{x_\alpha^2 + y_\alpha^2}.$$

Here we have used the fact that function $h(\alpha, \alpha') \sim \mathcal{O}(\alpha - \alpha')$. Thus, the second piece on the right-hand side of (3.9) is also smooth and has a removable singularity, and $g_2(\alpha, \alpha')$ can be evaluated using a standard composite trapezoidal rule. Similar to the singular piece in the single-layer term, the singular piece on the right-hand side of (3.9) again can be evaluated using the quadrature given by (3.7).

To summarize, using the collocation method with the quadrature rules described above, the boundary integral equation (3.4) is discretized into a dense linear system of equations, which can be solved using an iterative solver, e.g., GMRES. Because (3.4) is well-conditioned, no preconditioner is needed. In particular, for the computations shown in section 4.3, the number of iterations for GMRES is about 7 at early times and is about 20 at later times as the interface gets complicated. We find that the number of iterations for GMRES is independent of the number of unknowns N once the interface is well resolved. Once the adatoms density is solved, we can easily evaluate the normal velocity using (2.13) and (2.14). The main computational cost comes from the matrix-vector multiplication in GMRES. Currently we use direct summation to compute the product. As a result, the operation count is essentially $\mathcal{O}(N^2)$, where N is the total number of calculation points. Using a fast multipole method we can reduce the computation cost down to $\mathcal{O}(N)$ or $\mathcal{O}(N \log N)$. At our current resolutions (especially for the shrinking island cases), we find it sufficient to use direct summation, though it is expensive. We will implement the fast multipole method to study growing dynamics involving large numbers of points.

3.3. Interface evolution.

3.3.1. Dynamics. Consider a point $\mathbf{x}(\alpha, t) = (x(\alpha, t), y(\alpha, t)) \in \Sigma(t)$, where $\Sigma(t)$ is the island boundary. Suppose the normal velocity is calculated using (2.14). Denote the tangent velocity by $T(\alpha, t)$ and notice that the morphology of the interface is independent of $T(\alpha, t)$. Following [39, 42, 40], we choose the following $T(\alpha, t)$ that ensures the equal arclength distribution of grid points to prevent local clustering of computation points on the interface:

$$(3.13) \quad T(\alpha, t) = T(0, t) + \int_0^\alpha s'_\alpha \kappa' V d\alpha' - \frac{\alpha}{2\pi} \int_0^{2\pi} s'_\alpha \kappa' V d\alpha';$$

the motion of $\Sigma(t)$ is given by

$$(3.14) \quad \frac{d}{dt} \mathbf{x}(\alpha, t) = V(\alpha, t) \mathbf{n} + T(\alpha, t) \mathbf{s}.$$

Note that using the equal arclength scheme, we have identity $ds = \frac{L}{2\pi} d\alpha$ (i.e., the collocation points are equally spaced along the interface), where $L(t)$ is the length of the island boundary $\Sigma(t)$. Using the equal arclength frame, we may naturally repose the equations of motion in terms of the tangent angle and the arclength of the interface:

$$(3.15) \quad \theta_t = V_s + \kappa T,$$

$$(3.16) \quad s_{\alpha t} = (T_s - \kappa V) s_\alpha.$$

The position vector \mathbf{x} can be reconstructed by simply integrating

$$(3.17) \quad \mathbf{x}_\alpha = \frac{L(t)}{2\pi} (\cos \theta(\alpha, t), \sin \theta(\alpha, t)).$$

3.3.2. Small-scale decomposition. The idea of the small-scale decomposition (SSD) is to extract the dominant part of the equations at small spatial scales [39]. SSD has been successfully implemented in the context of the Hele–Shaw problem [39, 40, 41], precipitate evolution in an elastic matrix [42], and dynamics of inextensible vesicles [43].

Through the boundary condition at the interface (see, e.g., (2.13)), the line tension introduces high-order terms, both nonlinear and nonlocal, into the dynamics. This leads to severe stability constraints for explicit time integration methods. To remove the stiffness, we use SSD in our problem and develop an explicit, nonstiff time integration algorithm. In (3.4), based on the analysis of the single-layer and double-layer terms, the only singularity in the integrands comes from the logarithmic kernel. Following [39] and noticing the curvature term in (2.13), one can show that at small spatial scales,

$$(3.18) \quad V(\alpha, t) \sim \frac{\rho^* \gamma}{s_\alpha^2} \mathcal{H}[\theta_{\alpha\alpha}],$$

where \mathcal{H} is the Hilbert transformation. We rewrite (3.15),

$$(3.19) \quad \theta_t = \frac{\rho^* \gamma}{s_\alpha^3} \mathcal{H}[\theta_{\alpha\alpha\alpha}] + N(\alpha, t),$$

where the Hilbert transform term is the dominating high-order term at small spatial scales, and $N = (V_s + \kappa T) - \frac{\rho^* \gamma}{s_\alpha^3} \mathcal{H}[\theta_{\alpha\alpha\alpha}]$ contains other, lower-order terms in the evolution. This demonstrates that an explicit time-stepping method has the high-order constraint $\Delta t \leq \left(\frac{h}{s_\alpha}\right)^3$, where Δt and h are the time step and spatial grid size, respectively. This has been demonstrated numerically in the seminal work [39] for a Hele–Shaw problem, and more recently in [43] for an inextensible vesicle problem. For the epitaxial problem, the semi-implicit time integration scheme (see (3.19)) requires $\Delta t = O(h)$, instead of $\Delta t = O(h^3)$ for an explicit scheme. In section 4.3, we show a numerical example using $N = 512$ to simulate a 5-fold star-shaped island. In this simulation, we can use Δt as large as $\Delta t = 1.0 \times 10^{-2}$ for stability, instead of $\Delta t < 10^{-6}$ for an explicit scheme. For the purpose of numerical accuracy, we used a smaller time step in our simulations.

Taking the Fourier transform of (3.19), we get

$$(3.20) \quad \hat{\theta}_t = -\frac{\rho^* \gamma |k|^3}{s_\alpha^3} \hat{\theta}(k, t) + \hat{N}(k, t).$$

We solve (3.20) using the second-order accurate linear propagator method in the Adams–Bashforth form [39] in Fourier space and apply the inverse Fourier transform to recover θ . Specifically, we discretize (3.20) as

$$(3.21) \quad \hat{\theta}^{n+1}(k) = e_k(t_n, t_{n+1}) \hat{\theta}^n(k) + \frac{\Delta t}{2} (3e_k(t_n, t_{n+1})) \hat{N}^n(k) - e_k(t_{n-1}, t_{n+1}) \hat{N}^{n-1}(k),$$

where the superscript n denotes the numerical solutions at $t = t_n$ and the parameter

$$e_k(t_1, t_2) = \exp\left(-\rho^* \gamma |k|^3 \int_{t_1}^{t_2} \frac{dt}{s_\alpha^3(t)}\right).$$

The integrals in (3.21) can be evaluated simply using a trapezoidal rule,

$$\int_{t_n}^{t_{n+1}} \frac{dt}{s_\alpha^3(t)} \approx \frac{\Delta t}{2} \left(\frac{1}{(s_\alpha^n)^3} + \frac{1}{(s_\alpha^{n+1})^3} \right),$$

$$\int_{t_{n-1}}^{t_{n+1}} \frac{dt}{s_\alpha^3(t)} \approx \Delta t \left(\frac{1}{2(s_\alpha^{n-1})^3} + \frac{1}{(s_\alpha^n)^3} + \frac{1}{2(s_\alpha^{n+1})^3} \right).$$

To compute the arclength s_α , equation (3.16) is solved using the explicit second-order Adams–Bashforth method [39],

$$(3.22) \quad s_\alpha^{n+1} = s_\alpha^n + \frac{\Delta t}{2}(3M^n - M^{n-1}),$$

where M is calculated using

$$M = -\frac{1}{2\pi} \int_0^{2\pi} V(\alpha, t) \theta_\alpha d\alpha.$$

Note that the linear propagator and Adams–Bashforth methods are multistep methods and require two previous time steps. The first time step is realized using an explicit Euler method. To reconstruct the island boundary $(x(\alpha, t), y(\alpha, t))$, we solve (3.17) and set the reference point to $(x(0, t), y(0, t))$, which is updated again using the Adams–Bashforth method.

We use a 25th-order Fourier filter to damp the highest nonphysical mode and suppress the aliasing error [39]. We also use Krasny filtering [46] to prevent the accumulation of roundoff errors during the computation.

4. Results and discussions. In this section, we validate the numerical algorithm and investigate the nonlinear evolution of the island. Unless otherwise specified, all numerical tests and simulations are performed using an equilibrium adatom density $\rho^* = 1.0$, the nondimensional kinetic coefficient $\xi_- = 1.0$, the nondimensional line tension $\gamma = 0.01$, and desorption rate $\mu = 2.5$. With these parameters, the critical deposition flux at $t = 0$ can be easily calculated to be $\Lambda^c = 6.31$ from (2.23). The error tolerance for GMRES is set to be 10^{-12} and the 25th-order Fourier smoothing with the filter level 10^{-13} is used. All simulations are performed on a single core of Dell desktop with CPU speed 3.0GHz.

4.1. Accuracy test. We first test the accuracy of our numerical computations by considering the evolution of a circular island with initial radius $R(0) = 1.0$. We compare our numerical results for the normal velocity and the modified adatom density with analytical solutions presented in (2.18) and (2.17). We set the number of mesh points to be $N = 256$ along the interface and the time step $\Delta t = 1.0 \times 10^{-3}$.

In this calculation, we choose two fluxes: $\Lambda = 6.5 > \Lambda^c$ (growth) and $\Lambda = 5.0 < \Lambda^c$ (shrinkage) and run the simulation up to final time $T = 0.4$. During evolution, the island remains circular. In Figure 1(a) and (b), we plot the normal velocity of the island versus time. It is evident that both growth and shrinkage cases are in excellent agreement with the analytical predictions. In particular, at the final time $T = 0.4$, we found at least ten digits after the decimal point are in agreement with analytical solutions, which is close to the GMRES tolerance. Analogous results hold for the adatom density ω as well.

We next test the accuracy of the numerical methods for solving the boundary integral equation (3.3). We use an analytical solution, $\omega(\mathbf{x}) = \Phi_0(\mathbf{x}, 0) = -K_0(\mu|\mathbf{x}|)/2\pi$,

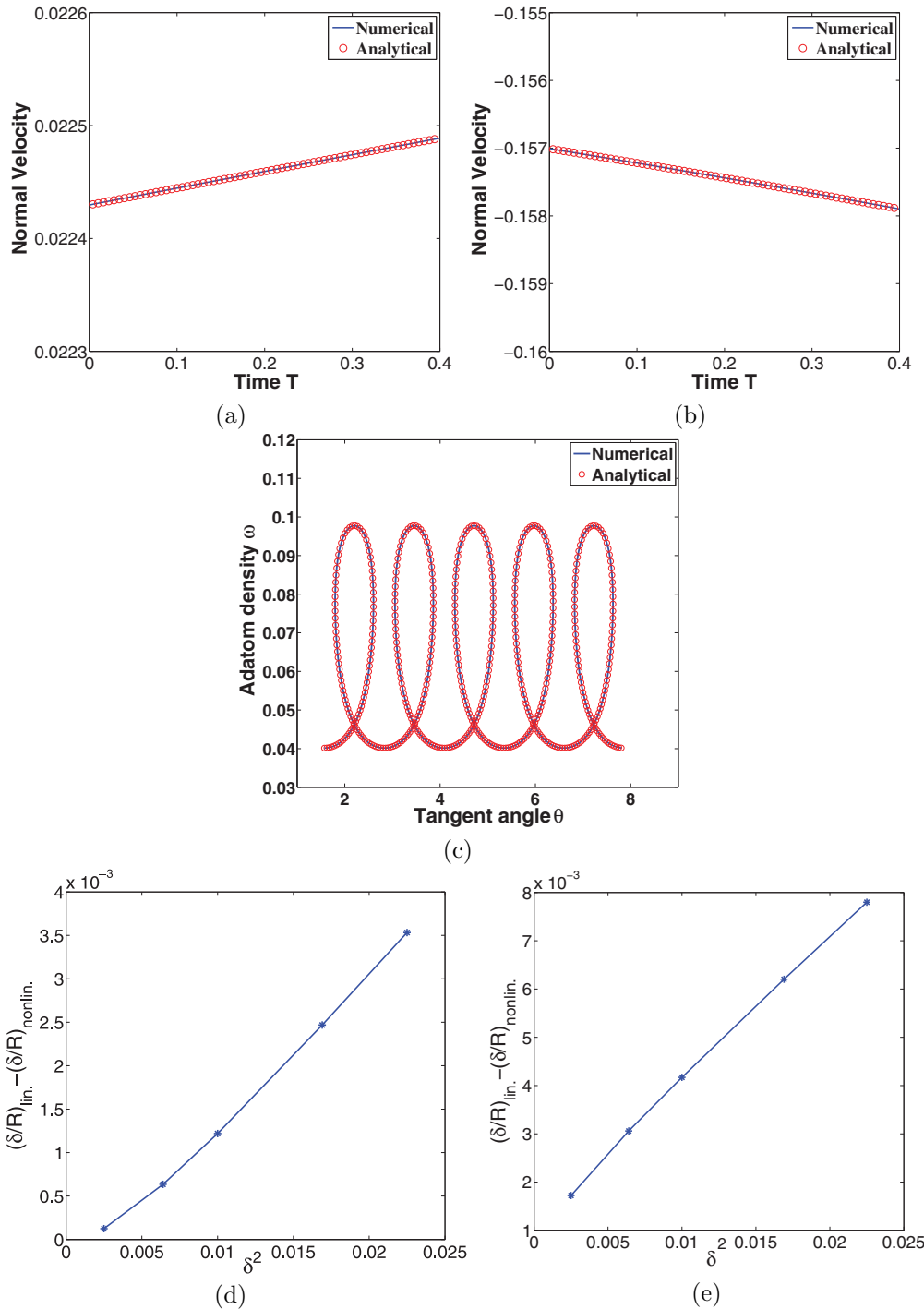


FIG. 1. The accuracy study of the boundary integral method. The initial shape is chosen to be a unit circle. (a) shows the growth of the circular island. (b) shows the shrinkage of the circular island. (c) shows the accuracy of the integral solver for a perturbed circle, $r(\alpha, 0) = 1.0 + 0.15 \cos(5\alpha)$. (d) and (e) show the difference between the linear solution and nonlinear solution. The initial shape is a perturbed circle with $r(\alpha, 0) = 1.0 + \delta(0) \cos(5\alpha)$. In this calculation, we vary the perturbation amplitude, $\delta(0) = 0.05, 0.08, 0.10, 0.13$, and 0.15 .

to the modified Helmholtz equation (2.12) to test our numerical calculations. Note that the boundary condition (2.13) becomes

$$(4.1) \quad \xi_- \nabla \omega \cdot \mathbf{n} = \omega + \frac{1}{2\pi} \left[\xi_- \mu K_1(\mu|\mathbf{x}|) \frac{\mathbf{x}}{|\mathbf{x}|} \cdot \mathbf{n} + K_0(\mu|\mathbf{x}|) \right] \quad \text{for } \mathbf{x} \in \Sigma(t).$$

The analytical solution $\omega(\mathbf{x}) = -K_0(\mu|\mathbf{x}|)/2\pi$ satisfies the far-field condition (2.15), as well as (3.3) with the right-hand side replaced by

$$-\frac{1}{2\pi} \int_{\Sigma(t)} \xi_-^{-1} \left[\xi_- \mu K_1(\mu|\mathbf{x}'|) \frac{\mathbf{x}'}{|\mathbf{x}'|} \cdot \mathbf{n}(\mathbf{x}') + K_0(\mu|\mathbf{x}'|) \right] \Phi_0(\mathbf{x}, \mathbf{x}') \, ds(\mathbf{x}').$$

In Figure 1(c), we demonstrate the agreement between the analytical solution $\omega(\mathbf{x}) = \Phi_0(\mathbf{x}, 0) = -K_0(\mu|\mathbf{x}|)/2\pi$ and the numerical results from the integral solver. The maximum difference is around machine precision. In this calculation, we use $N = 512$ points on the interface and plot the adatom density against the tangent angle. The interface is taken to be a perturbed circle, $r(\alpha, 0) = 1.0 + 0.15 \cos(5\alpha)$.

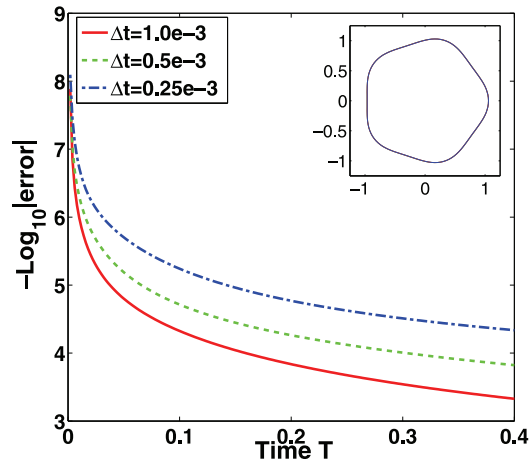
Next, we consider the evolution of a perturbed circular island. The initial shape is taken to be $r(\alpha, 0) = 1.0 + \delta(0) \cos(5\alpha)$. In this calculation, we vary the perturbation amplitude, $\delta(0) = 0.05, 0.08, 0.10, 0.13$, and 0.15 , and run simulations up to the final time $T = 0.1$. The deposition fluxes used are $\Lambda = 6.5$ (growth) and $\Lambda = 5.0$ (shrinkage). Other parameters are the same as those used to produce Figure 1(a). In Figure 1(d) and (e), we plot the difference of the shape factor (quantity δ/R) at the final time between the linear theory and nonlinear simulations versus the square of $\delta(0)$. In the linear theory, the shape factor δ/R can be obtained by solving (2.18) and (2.24) using an ODE solver. In the nonlinear computation, the quantity δ/R is calculated numerically by

$$(4.2) \quad \delta/R = \max \|\mathbf{x}\|/R_{\text{eff}} - 1,$$

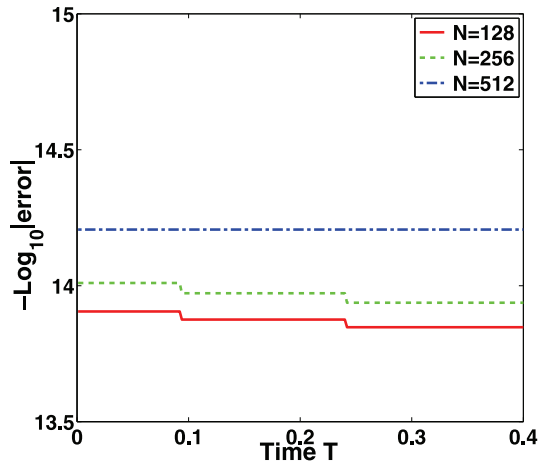
where \mathbf{x} is the position vector from the centroid of the shape to the interface and R_{eff} is the effective radius of the nonlinear shape. In Figure 1(d) (shrinkage) and (e) (growth), the deviation of the nonlinear results from linear theory is quadratic in $\delta(0)$, as expected. Analogous results (not shown) were found to hold for any other k -fold perturbed shapes as well.

4.2. Convergence test. As we have demonstrated in the previous section, the boundary integral method itself is accurate when comparing with analytical solutions. In this section, we test the convergence of the method. We first perform a temporal resolution study. We consider the evolution of a perturbed circular island with initial shape $r(\alpha, 0) = 1.0 + 0.05 \cos(5\alpha)$. In this calculation, we choose the number of mesh points to be $N = 256$ and the deposition flux to be a constant $\Lambda = 6.5$ (growth) or $\Lambda = 5.0$ (shrinkage). For brevity, we only present the growth case.

We use a computation with $\Delta t = 0.125 \times 10^{-3}$ to approximate the exact solution and compare the solution to those using $\Delta t = 1.0 \times 10^{-3}$, 0.5×10^{-3} , and 0.25×10^{-3} . The error is measured in the arclength difference, i.e., $\text{error} = |L(t) - L^*(t)|$, where $L^*(t)$ is the arclength computed using time step $\Delta t = 0.125 \times 10^{-3}$. Figure 2(a) shows the base 10 logarithm of the temporal error plotted versus the computation time t . The distance between these curves uniformly decreases by a factor of 0.6 with each halving of the time step, and this confirms the second-order accuracy, which is consistent with the second-order Adams–Bashforth scheme we used to evolve the interface. The



(a)



(b)

FIG. 2. Convergence study of the boundary integral method. The initial shape is chosen to be $(x(\alpha, 0), y(\alpha, 0)) = r(\alpha, 0)(\cos \alpha, \sin \alpha)$ with $r(\alpha, 0) = 1.0 + 0.05 \cos 5\alpha$. (a) shows the second-order convergence in time, and (b) shows the spatial resolution study. The time step is set to be $\Delta t = 1.0 \times 10^{-4}$.

morphologies of the islands corresponding to different temporal resolution at $T = 0.35$ are shown as an inset. The difference between these morphologies is indistinguishable. We note that the scheme is stable and still quite accurate using even much larger time steps.

We next test the spatial resolution and confirm the spectral accuracy in space. We use a computation with $N = 1024$ to approximate the exact solution and compare the solution to those using 128, 256, and 512. We set the deposition flux $\Lambda = 6.5$. For all computations, we choose $\Delta t = 1.0 \times 10^{-4}$. As in the temporal case, the error is again measured as $error = |L(t) - L^*(t)|$, where $L^*(t)$ is the arclength computed using spatial resolution $N = 1024$. Figure 2(b) shows the base 10 logarithm of the

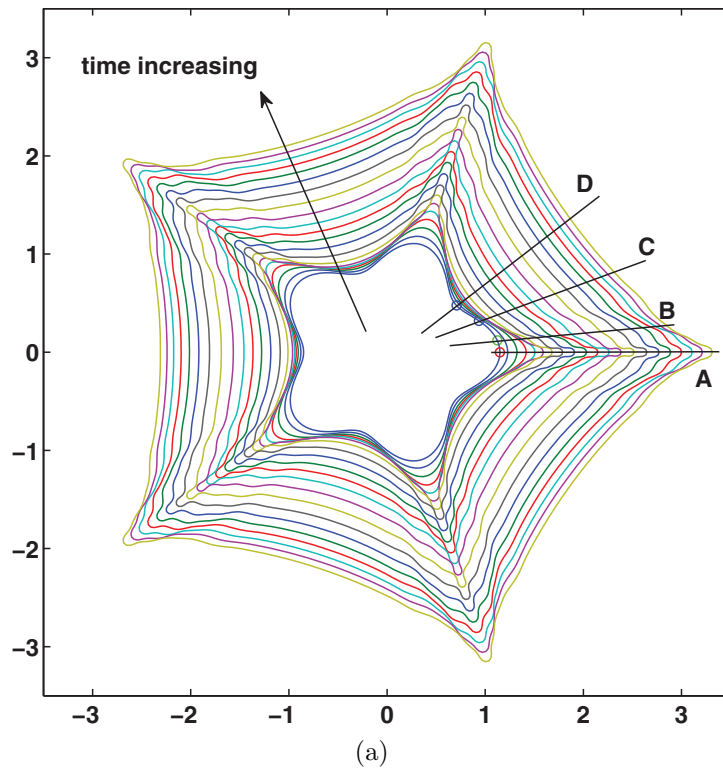


FIG. 3. Evolution of a 5-fold star shape with $\Lambda = 500, \mu = 2.5$. The initial shape is chosen to be $(x(\alpha, 0), y(\alpha, 0)) = r(\alpha, 0)(\cos \alpha, \sin \alpha)$, where $r(\alpha, 0) = 1.0 + 0.15 \cos 5\alpha$. Time step $\Delta t = 1.25 \times 10^{-4}$. The resolution $N = 512$ is used throughout the calculation. (a) shows the detailed evolution sequences. We show outputs from initial time $T = 0$ to final time $T = 0.03$ every 12 time steps.

space error plotted versus computation time t . We notice that even for $N = 128$ there are at least 12 digits of accuracy, which is around the GMRES tolerance. Increasing N from 256 to 512 does not improve the accuracy very much.

Putting all of this direct quantitative evidence together, the results strongly suggest that the developed numerical method is convergent and accurate.

4.3. Nonlinear growth a star-shaped island. In this section, we present simulations of a star-shaped island evolving into the nonlinear regime. We still use the desorption rate $\mu = 2.5$ and apply a deposition flux $\Lambda = 500$. The computation started with mesh points $N = 512$, which is found to be enough to resolve the interface during evolution. Figure 3(a) shows the growth of an island with initial shape $r(\alpha, 0) = 1.0 + 0.15 \cos(5\alpha)$. At the final computation time $T = 0.03$, the equivalent radius is around $R_{\text{eff}} = 2.6$. The total CPU time is about 150 minutes on the Dell desktop with CPU speed 3.0GHz. It is evident that the island evolves into a compact, 5-fold sector-like morphology. During growth, the trough region evolves into a flat front indicating the formation of nearly straight edges; and there are wave-like fronts produced around the tip regions suggesting that meandering instability does occur. These morphologies (especially the formation of straight edges) are in qualitative agreement with the experimental observations of germanium islands growing on a silicon substrate [50]. The usual tip-splitting events which are very common in isotropic Laplacian growth

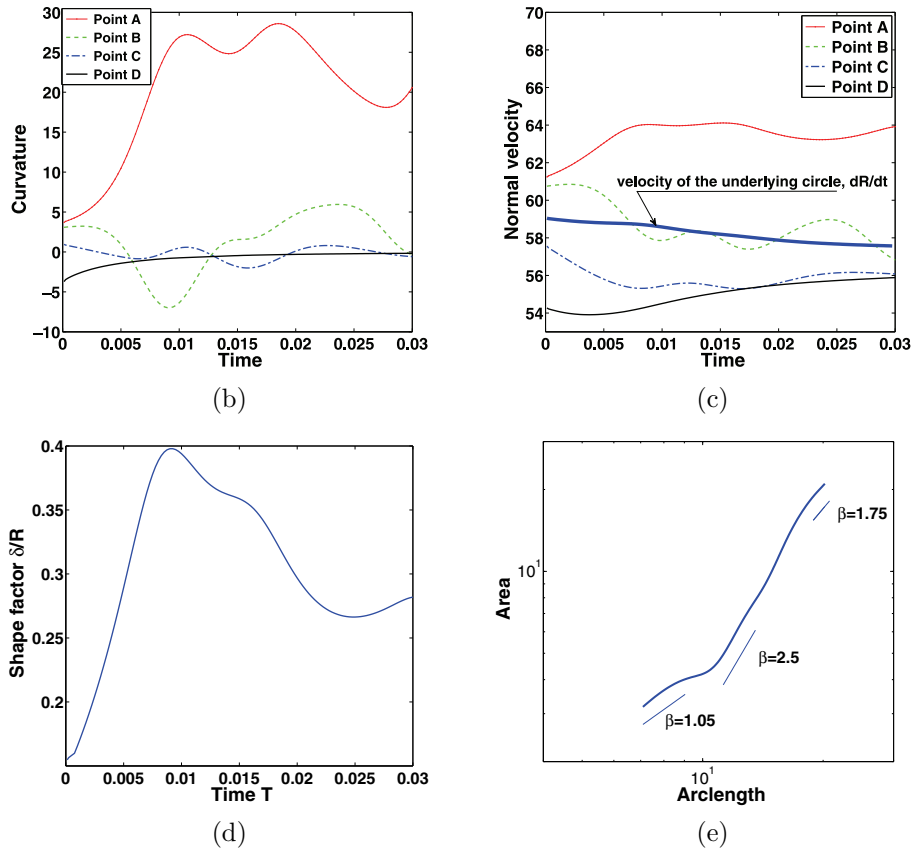


FIG. 3. (b) The evolution of curvature at points A, B, C, and D marked in (a). (c) The evolution of normal velocity at points A, B, C, and D. (d) The nonlinear evolution of shape factor δ/R . (e) Nonlinear growth of the area versus the arclength of the island boundary.

[40, 41] do not happen here. Similar results (not shown) were found to hold for other values of Λ with $\Lambda > \Lambda^c$ as well.

The step meandering instability was originally studied by Bales and Zangwill [16] for a train of straight steps. They showed that these steps may become morphologically unstable in the presence of a kinetic attachment asymmetry at the step due to the Ehrlich–Schwoebel effect. However, for an island, LRV showed that in the linear regime [25], when the line tension is present, islands are always stable. Our model, which is slightly different from the LRV model in terms of the diffusional domain, indicates that islands are stable subject to an applied flux $\Lambda > \Lambda^c$ shown in (2.24). This implies that the Bales–Zangwill instability for straight steps due to the kinetics mismatch does not occur for the island dynamics. Our nonlinear results for a perturbed island go beyond the linear predictions, and the meandering interface indicates that Bales–Zangwill instability occurs in the nonlinear regimes.

In Figure 3(b), we plot the curvature of the island boundary at points A, B, C, and D (marked in Figure 3(a)) versus time. It is evident that at point A (the tip point), the curvature increases rapidly at early times and starts to oscillate at $t = 0.01$. Note that during shape evolution, the curvature value at point A is the largest and remains positive, indicating there is no tip-splitting. Point B is close to

point A and has a positive curvature at $t = 0$. During evolution, the curvature at point B also shows oscillatory behavior, and in particular the value becomes negative at times $0.006 < t < 0.014$ indicating the neighborhood around B evolves from convex (at $t = 0$) to concave, i.e., the formation of a wave-like front. The point C, which is initially a bit far from the tip, shows small oscillations around curvature $\kappa = 0$, i.e., a flat front. Point D initially locates at the center of the concave trough region with the largest negative curvature; during evolution its value converges to zero monotonically, indicating the formation of a straight edge.

In Figure 3(c), we plot the normal velocity of the island boundary at points A, B, C, and D versus time. The solid thick line is the value of $\frac{dR}{dt}$ predicted by the linear theory in (2.18). At early times (up to $t = 0.01$), the normal velocities at point A and B are larger than the value of $\frac{dR}{dt}$, which measures the velocity of evolving front in an average sense. This implies the perturbation grows, as shown in Figure 3(d), where the shape factor δ/R increases rapidly from 0.155 at $t = 0.0$ to 0.395 at $t = 0.01$. After $t = 0.01$, the velocity at point A starts to oscillate, and the velocity at point B slows down with its value even below the dR/dt . Clearly in Figure 3(d), we observe the oscillatory behavior of δ/R , in particular a drop in the value of the shape factor after $t = 0.01$. The normal velocities at points C and D are always smaller than $\frac{dR}{dt}$, and at later times their values are almost equal. Notice that the normal velocity at point D keeps increasing after $t = 0.01$, indicating that more and more adatoms attached to the trough region and leading to the formation of a flat edge.

In Figure 3(e), the area $A(t)$ is shown versus arclength $L(t)$. There are two transitions connecting three roughly linear segments with different slopes marked along the $A(t)$ versus $L(t)$ curve. When $A(t)$ is small (at the early stages of growth), $A \sim L^{1.05}$. In this regime, the growth is characterized by the rapid growth of tip regions; i.e., the adatoms accumulate more to the tip regions instead of the trough regions. As the area increases, the first transition occurs at $L = 12$ and $A \sim L^{2.5}$. This regime is characterized by the rapid area growth of the island with more adatoms attached to the regions between tips. Notice the oscillatory behaviors of tip curvature and normal velocity in Figures 3(a) and 3(b). As a result, wave-like fronts (i.e., meandering instability) develop, as shown in Figure 3(a). The second transition from $A \sim L^{2.5}$ to $A \sim L^{1.75}$ occurs around $L = 35$ with $A = 28$. This indicates that the growth rate of the area decreases and suggests the formation of straight edges.

4.4. Nonlinear shrinking of an island. In this section, we present simulations of a shrinking island. We still use the desorption rate $\mu = 2.5$. To ensure the shrinking of the island, we apply a small deposition flux $\Lambda = 1.5$ during the calculation. The mesh points are set to be $N = 128$ along the island with initial shape $r(\alpha, 0) = 1.0 + 0.1(\sin 2\alpha + \cos 3\alpha - \cos 5\alpha)$. Figure 4(a) shows the island shrinks into a small circle and eventually disappears because of adatom desorption. At the final computation time $T = 1.55$, the equivalent radius is around $R_{\text{eff}} = 0.026$.

In Figure 4(b), we plot the curvature of points A, B, C, and D (marked in Figure 4(a)) versus time. It is evident that during evolution, the curvatures at these four different points converge to the same value after $t = 1.3$. At later times, the curvature increases rapidly (to infinity, not shown). This indicates that all perturbations are smoothed out and the island eventually vanishes. Note that points B and D (at convex regions with high frequencies) have higher curvature than points A and C (at concave regions). As a consequence, at early shrinking stages their shrinking velocities are larger than those of points A and C, shown in Figure 4(c). At later times (after $t = 1.3$), velocities of all four points converge to the same value predicted by (2.18)

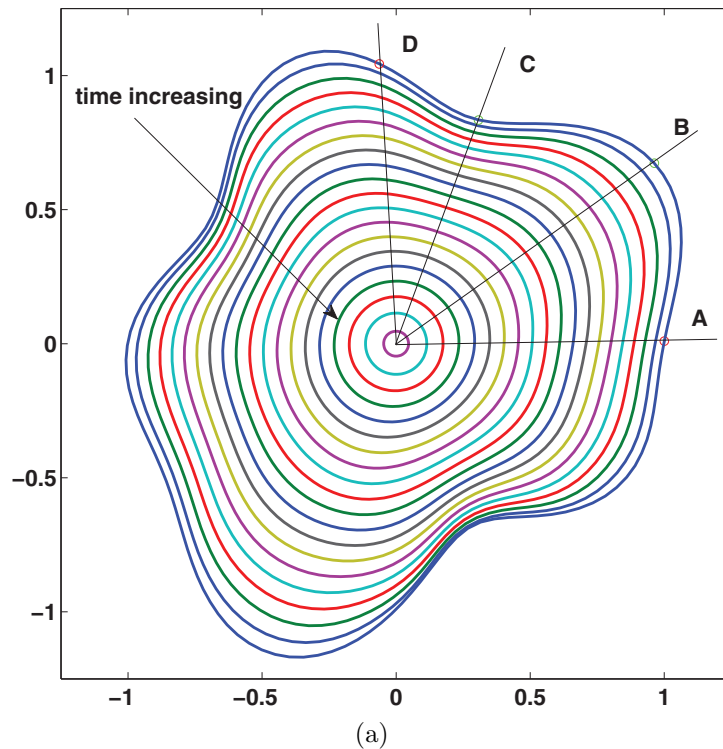


FIG. 4. Nonlinear simulation of a shrinking island with $\Lambda = 1.5$, $\mu = 2.5$. The initial shape is chosen to be $(x(\alpha, 0), y(\alpha, 0)) = r(\alpha, 0)(\cos \alpha, \sin \alpha)$, where $r(\alpha, 0) = 1.0 + 0.1(\sin 2\alpha + \cos 3\alpha - \cos 5\alpha)$. Time step $\Delta t = 1.25 \times 10^{-4}$. The resolution $N = 256$ is used throughout the calculation. (a) shows the detailed evolution sequences. We show outputs from initial time $T = 0$ to final time $T = 1.54$ every 640 time steps.

from the linear theory, which is marked by a solid thick line in Figure 4(c). In Figure 4(d), we confirm the rapid damping of perturbations. It is interesting to note that in Figure 4(e), the area of the shrinking island is scaled uniformly as $A \sim L^{2.0}$ during the evolution.

5. Conclusions. In this paper, we developed a boundary integral method for investigating the nonlinear growth/shrinkage of an island at its early growth stage. Numerical tests on a growing/shrinking circular island are in excellent agreement with the analytical solution and demonstrate that the method is stable, efficient, and spectrally accurate in space. Nonlinear simulations for the growth of perturbed circular islands show that sharp tips and flat edges will form during growth instead of the usual tip-splitting events for isotropic Laplacian growth. In particular, Bales-Zangwill instability is manifested in the form of wave-like fronts (meandering) around the tip regions. For a shrinking island, all perturbations are smoothed out and high wavenumbers (high curvature regions) are damped faster than the low wave frequencies.

In future work, we plan to include more physics (e.g., elasticity) into the model and characterize the nonlinear effects of elasticity on the evolution of islands and steps [52]. We will also extend our current work into multiple steps, i.e., a wedding-cake-like island. This would involve more computational work. In the last few years, many techniques for boundary integral methods have been developed. Examples include

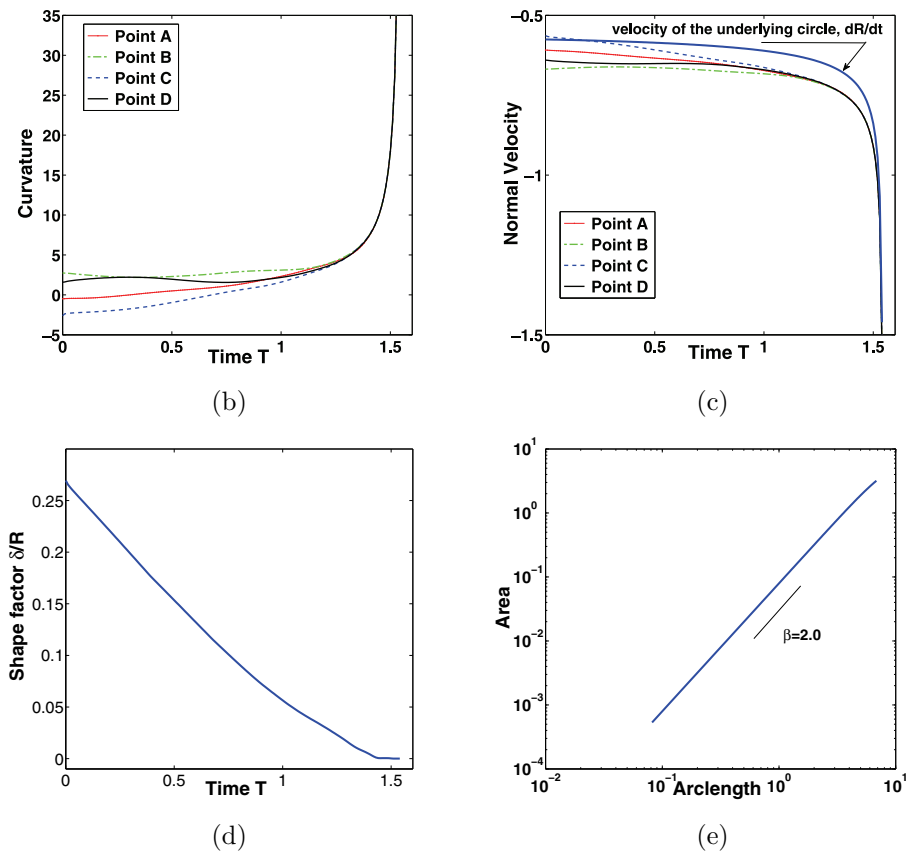


FIG. 4. (b) The evolution of curvature at points A, B, C, and D marked in (a). (c) The evolution of the normal velocity at points A, B, C, and D. (d) The evolution of the shape factor δ/R . (e) The evolution of the area of the island versus the arclength of the island boundary.

the fast multipole methods; see [34, 35, 56]. These techniques allow for more efficient evaluations of integrals. We will implement these techniques in our methods in the near future. The numerical techniques presented here can be applied generally to a class of free/moving boundary problems in physical and biological science; see [53] for the computation of a nutrition field around a tumor and [54] for the computation of the Stokes flow.

Acknowledgment. The authors thank Drs. Dajiang Liu and J. Evans for stimulating discussions.

REFERENCES

- [1] A. PIMPINELLI AND J. VILLAIN, *Physics of Crystal Growth*, Cambridge University Press, Cambridge, UK, 1998.
- [2] I. V. MARKOV, *Crystal Growth for Beginners: Fundamentals of Nucleation, Crystal Growth, and Epitaxy*, World Scientific, Singapore, 2003.
- [3] K. MORGENSTERN, G. ROSENFELD, AND G. COMSA, *Decay of two-dimensional Ag islands on Ag(111)*, Phys. Rev. Lett., 76 (1996), pp. 2113–2116.
- [4] W. THEIS, N. C. BARTELT, AND R. M. TROMP, *Chemical potential maps and spatial correlations in 2D-island ripening on Si(001)*, Phys. Rev. Lett., 75 (1995), pp. 3328–3331.

- [5] A.-L. BARABÁSI AND H. E. STANLEY, *Fractal Concepts in Surface Growth*, Cambridge University Press, Cambridge, UK, 1995.
- [6] J. KRUG, *Four lectures on the physics of crystal growth*, Phys. A, 313 (2002), pp. 47–82.
- [7] W. K. BURTON, N. CABRERA, AND F. C. FRANK, *The growth of crystals and the equilibrium structure of their surfaces*, Philos. Trans. Roy. Soc. London Ser. A, 243 (1951), pp. 299–358.
- [8] J. W. EVANS, P. A. THIEL, AND M. C. BARTELT, *Morphological evolution during epitaxial thin film growth: Formation of 2D islands and 3D mounds*, Surface Sci. Rep., 61 (2006), pp. 1–128.
- [9] J. W. EVANS, D.-J. LIU, AND M. TAMMARO, *From atomistic lattice-gas Models for surface reactions to hydrodynamic reaction-diffusion equations*, Chaos, 12 (2002), pp. 131–143.
- [10] D.-J. LIU AND J. W. EVANS, *From atomic scale ordering to mesoscale spatial patterns in surface reactions: A heterogeneous coupled lattice-gas simulation approach*, Multiscale Model. Simul., 4 (2005), pp. 424–446.
- [11] R. E. CAFLISCH, W. E. M. F. GYURE, B. MERRIMAN, AND C. RATSCH, *Kinetic model for a step edge in epitaxial growth*, Phys. Rev. E, 59 (1999), pp. 68–79.
- [12] R. E. CAFLISCH AND B. LI, *Analysis of island dynamics in epitaxial growth of thin films*, Multiscale Model. Simul., 1 (2003), pp. 150–171.
- [13] C. RATSCH, M. F. GYURE, R. E. CAFLISCH, F. GIBOU, M. PETERSON, M. KANG, J. GARCIA, AND D. D. VVEDENSKY, *Level-set method for island dynamics in epitaxial growth*, Phys. Rev. B, 65 (2002), 195403.
- [14] R. E. CAFLISCH, M. F. GYURE, B. MERRIMAN, S. OSHER, C. RATSCH, D. D. VVEDENSKY, AND J. J. ZINCK, *Island dynamics and the level set method for epitaxial growth*, Appl. Math. Lett., 12 (1999), pp. 13–22.
- [15] S. CHEN, B. MERRIMAN, M. KANG, R. E. CAFLISCH, C. RATSCH, L. T. CHENG, M. GYURE, R. P. FEDKIW, C. ANDERSON, AND S. OSHER, *A level set method for thin film epitaxial growth*, J. Comput. Phys., 167 (2001), pp. 475–500.
- [16] G. S. BALES AND A. ZANGWILL, *Morphological instability of a terrace edge during step-flow growth*, Phys. Rev. B, 41 (1990), pp. 5500–5508.
- [17] F. LIU AND H. METIU, *Stability and kinetics of step motion on crystal surfaces*, Phys. Rev. E, 49 (1994), pp. 2601–2616.
- [18] O. PIERRE-LOUIS, *Continuum model for low temperature relaxation of crystal shapes*, Phys. Rev. Lett., 87 (2001), 106104.
- [19] Z. ZHANG AND M. G. LAGALLY, *Atomistic processes in the early stages of thin-film growth*, Science, 276 (1997), pp. 377–383.
- [20] Z. HU, S. LI, AND J. LOWENGRUB, *Morphological stability analysis of the epitaxial growth of a circular island: Application to nanoscale shape control*, Phys. D, 233 (2007), pp. 151–166.
- [21] F. HAUSSER AND A. VOIGT, *Finite element method for epitaxial island growth*, J. Crystal Growth, 266 (2004), pp. 381–387.
- [22] E. BÄNSCH, F. HAUSSER, O. LAKKIS, B. LI, AND A. VOIGT, *Finite element method for epitaxial growth with attachment-detachment kinetics*, J. Comput. Phys., 194 (2004), pp. 409–434.
- [23] A. RÄTZ AND A. VOIGT, *Various phase-field approximations for epitaxial growth*, J. Crystal Growth, 266 (2004), pp. 278–282.
- [24] F. OTTO, P. PENZLER, A. RÄTZ, T. RUMP, AND A. VOIGT, *A diffuse-interface approximation for step flow in epitaxial growth*, Nonlinearity, 17 (2004), pp. 477–491.
- [25] BO LI, A. RÄTZ, AND A. VOIGT, *Stability of a circular epitaxial island*, Phys. D, 198 (2004), pp. 231–247.
- [26] Z. HU, S. LI, S. WISE, J. LOWENGRUB, AND A. VOIGT, *Phase-field modeling of nanoscale island dynamics*, in Proceedings of TMS 2008 (137th meeting) Supplemental Proceedings: Materials Processing and Properties, 1 (2008), pp. 111–116.
- [27] E. BÄNSCH, F. HAUSSER, AND A. VOIGT, *Finite element method for epitaxial growth with thermodynamic boundary conditions*, SIAM J. Sci. Comput., 26 (2005), pp. 2029–2046.
- [28] Y. XIANG, *Derivation of a continuum model for epitaxial growth with elasticity on vicinal surface*, SIAM J. Appl. Math., 63 (2002), pp. 241–258.
- [29] G. EHRLICH AND F. G. HUDDA, *Atomic view of surface diffusion: Tungsten on tungsten*, J. Chem. Phys., 44 (1966), pp. 10–39.
- [30] R. L. SCHWOEBEL AND E. J. SHIPSEY, *Step motion on crystal surfaces*, J. Appl. Phys., 37 (1966), pp. 36–82.
- [31] B. LI AND J.-G. LIU, *Epitaxial growth without slope selection: Energetics, coarsening, and dynamic scaling*, J. Nonlinear Sci., 14 (2004), pp. 429–451.
- [32] Y. GONG, B. LI, AND Z. LI, *Immersed-interface finite-element methods for elliptic interface problems with nonhomogeneous jump conditions*, SIAM J. Numer. Anal., 46 (2008), pp. 472–495.

- [33] J. HUANG, M. C. LAI, AND Y. XIANG, *An integral equation method for epitaxial step-flow growth simulations*, J. Comput. Phys., 216 (2006), pp. 724–743.
- [34] H. CHENG, J. HUANG, AND T. J. LEITERMAN, *An adaptive fast solver for the modified Helmholtz equation in two dimensions*, J. Comput. Phys., 211 (2006), pp. 616–637.
- [35] M. C. KROPINSKI AND B. QUAIFFE, *Fast integral equation methods for the modified Helmholtz equation*, J. Comput. Phys., 230 (2011), pp. 425–434.
- [36] S. OSHER AND J. A. SETHIAN, *Front propagating with curvature-dependent speed: Algorithms based on Hamilton–Jacobi formulations*, J. Comput. Phys., 79 (1988), pp. 12–49.
- [37] W. W. MULLINS AND R. F. SEKERKA, *Morphological stability of a particle growing by diffusion or heat flow*, J. Appl. Phys., 34 (1963), pp. 323–329.
- [38] D. JURIC AND G. TRYGGVASON, *A front tracking method for dendritic solidification*, J. Comput. Phys., 123 (1996), pp. 127–148.
- [39] T. Y. HOU, J. S. LOWENGRUB, AND M. J. SHELLEY, *Removing the stiffness from interfacial flows with surface tension*, J. Comput. Phys., 114 (1994), pp. 312–338.
- [40] S. LI, J. LOWENGRUB, AND P. LEO, *A rescaling scheme with application to the long time simulation of viscous fingering in a Hele-Shaw cell*, J. Comput. Phys., 225 (2007), pp. 554–567.
- [41] S. LI, J. LOWENGRUB, J. FONTANA, AND P. PALFFY-MUHORAY, *Control of viscous fingering patterns in a radial Hele-Shaw cell*, Phys. Rev. Lett., 102 (2009), 174501.
- [42] H. J. JOU, P. LEO, AND J. LOWENGRUB, *Microstructural evolution in inhomogeneous elastic media*, J. Comput. Phys., 131 (1997), pp. 109–148.
- [43] J.-S. SOHN, Y.-H. TSENG, S. LI, J. LOWENGRUB, AND A. VOIGT, *Dynamics of multicomponent vesicles in a viscous fluid*, J. Comput. Phys., 229 (2010), pp. 119–144.
- [44] R. KRESS, *On the numerical solution of a hypersingular integral equation in scattering theory*, J. Comput. Appl. Math., 61 (2005), pp. 345–360.
- [45] J. SETHIAN, *Level Set Methods*, Cambridge University Press, Cambridge, UK, 1996.
- [46] R. KRASNY, *A study of singularity formation in a vortex sheet by the point vortex approximation*, J. Fluid Mech., 167 (1986), pp. 65–93.
- [47] A. ZANGWILL, *Physics at Surfaces*, Cambridge University Press, Cambridge, UK, 1988.
- [48] K. R. ROOS, K. L. ROOS, I. LOHMAR, D. WALL, J. KRUG, M. HORN-VON HOEGEN, AND F.-J. MEYER ZU HERINGDORF, *Real-time view of mesoscopic surface diffusion*, Phys. Rev. Lett., 100 (2008), 016103.
- [49] P. PEYLA, A. PIMPINELLI, J. CIBERT, AND S. TATARENKO, *Deposition and growth with desorption for CdTe molecular beam epitaxy*, J. Crystal Growth, 184-185 (1998), pp. 75–79.
- [50] A. SGARLATA, P. D. SZKUTNIK, A. BALZAROTTI, N. MOTTA, AND F. ROSEI, *Self-ordering of Ge islands on step-bunched Si(111) surfaces*, Appl. Phys. Lett., 83 (2003), pp. 4002–4004.
- [51] Y. SAAD AND M. H. SCHULTZ, *GMRES: A generalized minimal residual algorithm for solving nonsymmetric linear systems*, SIAM J. Sci. Statist. Comput., 7 (1986), pp. 856–869.
- [52] D. YEON, P. CHA, J. LOWENGRUB, A. VOIGT, AND K. THORNTON, *Linear stability analysis for step meandering instabilities with elastic interactions and Ehrlich-Schwoebel barriers*, Phys. Rev. E, 76 (2007), 011601.
- [53] V. CRISTINI, J. LOWENGRUB, AND Q. NIE, *Nonlinear simulation of tumor growth*, J. Math. Biol., 46 (2003), pp. 191–224.
- [54] X. SUN AND X. LI, *A spectrally accurate boundary integral method for interfacial velocities in two-dimensional Stokes flow*, Commun. Comput. Phys., 8 (2010), pp. 933–946.
- [55] B. K. ALPERT, *Hybrid Gauss-trapezoidal quadrature rules*, SIAM J. Sci. Comput., 20 (1999), pp. 1551–1584.
- [56] M. C. KROPINSKI, *An efficient numerical method for studying interfacial motion in two-dimensional creeping flows*, J. Comput. Phys., 171 (2001), pp. 479–508.